Irregular Insertion of Lithium Ions into Graphite

Na Li[1, 2], Mingzi Sun[3], Sooyeon Hwang[2], Shuang Li[2], Hongyang Zhao[1], Yaping Du[4]*, Bolong Huang[3]*, Dong Su[2, 5]*

[1] Key Laboratory of Shaanxi for Advanced Materials and Mesoscopic Physics, School of Physics, Xi'an Jiaotong University, No. 28 West Xianning Road, Xi'an 710049, China.
[2] Center for Functional Nanomaterials, Brookhaven National Laboratory, Upton, New York 11973, United States.
[3] Department of Applied Biology and Chemical Technology, The Hong Kong Polytechnic University, Hong Hum, Kowloon, Hong Kong SAR, China.
[4] School of Materials Science and Engineering & National Institute for Advanced Materials, Nankai University, Tianjin 300350, China.
[5] Beijing National Laboratory for Condensed Matter Physics, Institute of Physics, Chinese Academy of Sciences, Beijing, 100190, China.

[#] Na Li, and Mingzi Sun contributed equally to this work.

Emails: ypdu@nankai.edu.cn, bhuang@polyu.edu.hk, dsu@bnl.gov

Abstract

Graphite has been regarded as the most important anode material for lithium-ion batteries due to its two-dimensional (2D) nature hosting ionic intercalations. However, the microscopic scenario of insertion of Li-ions is still well known. In this work, we investigated the real-time intercalation process of Li-ions using in-situ transmission electron microscopy. We observed the lithium insertion process at atomic scale where the graphite layers undergo expansion, wrinkle and finally inhomogeneous crack as the Li-ions accumulation. Leveraging on the theoretical simulations, Li-ions migration driven by external electrical field results in the irreversible wrinkled structures. This non-equilibrium behavior happened in lithium-ion batteries can be severe at a high charging rate, which will practically degrade the capacity of graphite. This work unveils the reaction scenario of the non-equilibrium Li-ions insertion, which benefits the understanding the performance of graphite-based energy-storage devices.

Introduction

Owing to the unique two-dimensional (2D) structure and high conductivity, graphite carbon has been utilized as the dominant anode for lithium-ion batteries (LIBs)[1]. In particular, two key processes determine the performances of graphite anode. The first is the reactions between graphite and designed electrolyte during the initial cycles, which prompt the formation of a stable and ionic conductive solid-electrolyte interphase (SEI) layer on the surface of the electrode. The second process is the intercalation and extraction of Li ions in graphite[2, 3]. Intensive investigations have been performed to study the intercalation of Li ions[3-9]. There are two generally accepted models for this process: Rüdorff-Hofmann (R-H) model explains that the stacking sequence of graphite layers shifts from ABAB in graphite (space group: $P6_3/mmc$) to AAAA in LiC_6 (space group: P6/mmm)[10, 11]; while Daumas-Herold (D-H) model considers the dynamics of the intercalation reaction, in which intercalants occupy the different gallery between pairs of graphite layers forming domains[6, 12, 13]. D-H model is regarded as accounting for the Li^+ intercalation process into graphite at a relatively slow rate limited by solid-state diffusion[14, 15].

However, the lithium ion intercalation to the graphite anode in a practical lithium battery involves essential differences from those two classic models. For example, the SEI layer formed on the surface of the electrode causes a potential drop between graphite and electrolyte (overpotential). At a relatively high rate, lithium metal deposited on the graphite surface and the surface overpotential propel surface Li ions into graphite[16, 17]. Previous Raman study proposed the side reactions may cause surface structural degradation of the graphite anode[18]. Very recently, an in-situ high-resolution transmission electron microscopy (TEM) study

revealed the existence of close-packed excess Li between two graphene sheets, contradicted to the predictions of R-H and D-H models[19]. This approach shed light to understand Li ions' insertion into graphite at the non-equilibrium conditions, however, up to now, it is not clear how surface overpotential affect the kinetics of intercalation in graphite[20].

In this work, we unveil the intercalation mechanism of lithium ions into graphite through the in-situ dry-cell TEM. In-situ high-resolution TEM (HRTEM), achieved at a spatial resolution of ~1.7 Å and a temporal resolution of ~0.2 s, shows evident proofs of distortion, wrinkle and cracking in the graphite layers. Theoretical simulations revealed the diffusion of Li-ions into graphite induced by the inhomogeneous Li ion migration under certain overpotential, identified at the graphite anode in coin cell by ex-situ HRTEM. This work revealed the novel structural evolution under the non-equilibrium condition in graphite anode refreshing our understanding of the critical issues governing the cyclability of lithium ion batteries.

Results and discussion

Fig. 1a shows the schematic of TEM dry cell used for this work[21-23]. The Li/Li_2O on a tungsten tip as anode were touching lacy carbon and the detailed experimental description can be found in the Methods section. To verify the dynamical process of Li ions insertion, we employed in-situ SAED to track the phase evolution during entire lithiation process, as shown in **Fig. 1** and **Supplementary Video S1**. **Fig. 1b** and **c** show the SAED patterns of pristine and fully lithiated samples, respectively, where we observed that after fully discharge, the graphite phase transfers to LiC_6, confirmed by the electron energy-loss spectroscopy (EELS) result (**Supplementary Fig. 1**) and ring-like patterns from Li_2O minor phase is also observed due to the possible reaction with surface impurities. The integrated intensity profiles of in-situ SAED from 0-7265 s are plotted in **Fig. 1d**. During lithiation, the shape of LiC_6 (001) peak is broadened and its

intensity becomes weak after 4211 s, which indicates the crystallization of the graphite layer languished after lithium intercalation. We identified of the lattice parameter. In the beginning, the graphite lattice along the ***c*** axis immediately extend, and the stages quickly changed from stage III to II. At 3930 s, the diffraction of stages I started to emerge, and stage II eventually transformed to stage I between 3930 s and 5559 s (**Fig. 1e**). Particularly, the transition from LiC_{12} to LiC_6 is indicated from the transformation of one single LiC_{12} (002) diffraction spot to the LiC_6 (001) peak (**Fig. 1f**) and the corresponding intensity change (**Fig. 1g**)[24].

To track the structural changes in real space at a higher rate, we performed in-situ high-resolution imaging with an aberration-corrected TEM (Titan 80-300). To speed up the reaction, the Li/Li_2O tip directly touched the graphite sample. Here the in-situ TEM imaging was taken at 80 kV and a low-dose rate (2.7×10^4 $e^-nm^{-2}s^{-1}$) to avoid the beam effects[25, 26]. **Fig. 2a** presents a time series of HRTEM images showing the evolution of a few graphite layers, captured during in-situ lithiation (**Supplementary Video S2**). A thin Li_2O layer was observed on the surface of graphite, serving as an inorganic SEI for following penetration of Li-ions. After an incubation time of ~150 s, the lattice of graphite started to show distortions at 156 s, and several cracks formed at 233 s. It is interesting that some distorted lattice can be recovered after initial lithiation, but the cracks cannot be recovered. **Fig. 2b** summarizes the reaction scenario for Li-ions' intercalation. The insertion of Li-ions can undergo stages predicted by the R-H model or D-H model, which account for the lithiation at an equilibrium state or a close to an equilibrium state. At higher reaction rate, the Li-ions may insert in neighboring spaces and expand adjacent carbon planes simultaneously, resulting in wrinkle or curved layers. With further lithium insertion, the formation of non-recoverable cracks was observed, which completely changes the reaction nature and modify the diffusion channel of 2D Li^+ intercalation.

We performed postmortem TEM analysis from the graphite electrodes tested in half-cell batteries at rates of 0.1 C and 10 C, respectively, to understand the structural change of graphite electrode after cycling. **Fig. 3a** shows the discharge profiles of 0.1 C and 10 C. The plateau above 0.5 V corresponds to Li ions adsorption on the surface or edge sites of graphite layers[27, 28], and the curve below 0.5 V (vs. Li/Li^+) is ascribed to the intercalation of Li-ions. **Fig. 3b** illustrates XRD patterns from pristine graphite, and the discharged samples after 10 cycles at 0.1 C and 10 C, respectively. LiC_6 phase is the dominated phase at two discharged states but a significant amount of LiC_{12} was observed in the sample at 10 C. In addition, from the Scherrer equation[29], the full width at half maximum (FWHM) of LiC_6 (001) peak shows the grain size, 51 nm and 33 nm for 0.1 C and 10 C samples, respectively (**Fig. 3b** and **Supplementary Fig. 2-3**)[30]. Additional analysis was performed with Raman spectroscopy (**Fig. 3c**), in which G-band peak at 1573 cm^{-1} and D-band peak at 1334 cm^{-1} were observed[31, 32]. It shows that the I_D/I_G ratio (0.91) of the sample at 10 C is higher than that at 0.1 C (0.75), indicating a lower degree of graphitization at the rate of 10 C. **Fig. 3d-f** presented the HRTEM images along the interlayer of pristine graphite, and the lithiated graphite samples under 0.1 C and 10 C after 10 cycles. The distorted graphite lattices, including wrinkle and cracks, were found in cycled samples. Inverse fast Fourier transform (IFFT) images from selected area are presented at insets. It is observed that graphite cycled at 10 C show a more severe distortion than that of 0.1C, in consistency with the results of XRD and Raman. HRTEM images were taken at multiple regions to ensure the statistical nature of the true reaction modalities (**Supplementary Fig. 4-6**). The bottom of **Fig. 3d-f** displayed the intensity profiles of Bragg reflection from FFT and showed the FWHM broaden with increasing of the charge rate (raw data was fitted by Lorentz fitting, **Supplementary Fig. 7**). The *ex-situ* analyses show the structural irregularity (wrinkles and

cracks) may relate to the charge rate or in practice, the current (**Fig. 3f**)[28].

In practice, high current may induce a high surface overpotential during the charge of the electrode[18]. Previous work suggested excess Li-ions could be deposited on the surface a higher charge rate and a high concentration of Li ions will swarm into graphite[16]. To understand the originality of the structural changes under this condition, we have performed density functional theory (DFT) based molecule dynamic (MD) calculation to unravel the actual mechanism of Li ions intercalation Under the applied overpotential along [010] direction, MD simulations clearly reveal the Li-ion migration behaviors in the graphite electrode, which significantly damaged the periodicity of graphite, supporting the distorted structure in in-situ TEM. The overall lithiation and delithiation process has been demonstrated under in Supplementary Fig. 8, which reveals the non-equilibrium lithiation condition with an external field and the delithiation process indicates the fully relaxed graphite structure after strongly distorted by the non-equilibrium lithiation. For more details of the non-equilibrium lithiation, we note that Li-ions are migrating towards one direction while the cracking occurs at the opposite edge (**Supplementary Fig. 9a**). Due to the strong distortion of graphite at one edge, the other edge leads to the tearing domain. The cracking edge maintains a relatively flat structure while the migration edge shows serious deformation as time increases. These types of edge morphologies are similar to the previous reports of zigzag and armchair edge characterized by STEM method[33]. In addition, the graphite cracking occurs in both NVT (*i.e. a dynamic study at fixed volume with a thermostat to maintain a constant temperature*) and NPT *(i.e. a dynamic study with a thermostat to maintain a constant temperature and with a barostat to maintain a constant pressure)* simulations, confirming the determining role of the Li-ion intercalation in the graphite distortion rather than the temperature or pressure effect. The significant increases of the C-C

bond length actually confirm the break C-C bonds in graphite, supporting the experimental observations for the graphite cracking phenomenon. (**Supplementary Fig. 9b**). Due to the quick and strong response to the local overpotential, the intercalations of Li ions destroy the interlayer van der Waals force, which significantly increases the instability of the local structure. Thus, the most distorted graphite region is attributed to more active Li ions than other regions. To reveal the tearing of the graphite, detailed quantification of the Li ions migrations in different regions are indicated, in which more active feature of Li ions near the graphite edge is noted (**Supplementary Fig. 9c**). To verify the reversibility of graphite structure during delithiation, we applied geometry optimization without an overpotential on the distorted graphite after removing all Li-ions. Notably, the graphite layer only preserved the partial graphite structure (**Supplementary Fig. 10**). The final structure after delithiation process undergoes the curve process to semi-sphere cage structures.

To compare with the condition with the electrical field, we have carried out the comparison simulations without any electrical field. **Extended Data Fig. S11** indicates that the neighboring layers of the graphite will migrate to opposite directions and become overlap induced by the lithium ions migration without electrical field. This behavior is consistent with the conventional R-H model. **Extended Data Fig. S12** further reveals the limited deformation of the graphite structure under MD without an external electrical field, which cannot support the experimental observations. Since the overall deformation of the graphite is very limited without an electrical field, we further track more details. **Extended Data Fig. S13** reveals the regular migration behaviors of lithium ions under two different initial model of simulations, supporting the conventional R-H models under the equilibrium condition. All these results confirm that non-equilibrium Li-ion migrations induced by overpotential is the dominant factor for the lattice

irregularity of graphite. By tracking the detailed C atoms migration of neighboring graphite layers, the opposite layer migration directions lead to the layer stacking changing from ABAB to AAAA as experimental results of R-H model[34]. The volume expansion induced by Li ions is noted (**Fig. 4a**). Initially, the volume of the unit cell immediately enlarges due to the formation of cracking. The repeated expansion and shrink are attributed to the stretching between layers. The following stable period of the volume expansion demonstrates the finish of cracking formation.

To further confirm the pivotal role of Li ions migrations to the lattice irregularity of graphite, we also investigate the formation of point defects in graphite. Generally, stone-wales defect, monovacancy, and divacancy are the most common defects in graphite that also supply a possible migration channel for interlayer Li ions diffusion. Among three types of defects, the Stone-wales defects have the lowest formation energy at 6.02 eV (**Fig. 4b**). In comparison, the formation energies of these defects reflect much higher energy cost than the formation of cracking. In previous works, the direct diffusion of Li ions through a graphite ring or defect has been proved to be very difficult[35, 36]. The energy comparison for the interlayer Li ions migrations further supported the more energetically preferred pathway of cracking rather than those point defects. For example, as shown in the **Fig. 4c**, for Li ions diffusion through the point defects such as divacancy defect, an obvious energy barrier of 1.60 eV is noticed. However, the migration of Li ions through the cracking only displays a nearly barrier-free migration path, indicating a highly favorable diffusion direction.

Therefore, the summarized demonstration of the discovered non-equilibrium lithiation/delithiation process is shown in **Fig. 4d**. During the lithiation, the swarm of Li ions to the graphite layers in a short time induces strong couplings with the graphite structures,

especially under high rate. The induced distortion firstly distorts the planar structure of the graphite layer, accompanied by the formation of curved fracture and cracks. The cracking of the graphite further opens the possibility of the inter-layer diffusion of Li ions beyond the conventional intra-layer diffusion. Such a non-equilibrium diffusion of the Li ions may cause the irreversible damage to the graphite layer. The graphite layer cannot completely recover to the well-ordered planar layer with partial preservation of the local graphite structure (**Supplementary Fig. 8, Fig. 10**). Such conclusion was evidenced by MD simulations. These structural irregularities may affect the performance of the graphite electrode: Excess lithium accumulated at the internal of distorted graphite but cannot contribute to the reversible capacity. After long cycles, the structural irregularities gradually form that evidentially decrease the reversible capacity of graphite in a practical cell.

In summary, we unveil the novel dynamics mechanism of lithium intercalation into graphite under the non-equilibrium state. Our high spatial and temporal resolution in situ TEM work reveals a completely new reaction scenario for the fast insertion of Li-ions into graphite interlayers. Beside observing curved graphite interlayers, cracks were observed during the lithiation process, which leads to irreversible structural changes for graphite anode. As verified by DFT-MD calculations, the cracked graphite interlayers were induced by the fast accommodation of excessive Li ions with the inhomogeneous response to the overpotential. These structure evidence with solid theoretical support confirmed the irregularity of graphite with loss of self-healing, reflecting the nature of non-equilibrium lithiation process. Our findings supply distinct insight into the microscopic ionic storage mechanism in two-dimensional layered materials.

Acknowledgments Electron microscopy work used resources of the Center for Functional Nanomaterials, which is a US DOE Office of Science Facility, at Brookhaven National Laboratory under Contract No. DE-SC0012704. We gratefully acknowledge the support from the program of China Scholarship Council, the China National Funds for Excellent Young Scientists (21522106), the National Key R&D Program of China (2017YFA0208000), the National Nature Science Foundation of China (21771156) and the Early Career Scheme (ECS) fund (Grant No.: PolyU 253026/16P) from the Research Grant Council (RGC) in Hong Kong. Thanks to Dr. Jing Li for her assistance on the in-situ TEM experiments.

Author Contributions Y. Du, B. Huang, and D. Su conceive the project. N. Li, S. Hwang, S. Li, H. Zhao, Y. Du and D. Su conducted the experiments. M. Sun and B. Huang conducted the theoretical calculations. N. Li and M. Sun contribute equally. All the authors contributed to the discussion and writing of the paper. Authors declare no competing interests. All data is available in the main text or the supplementary materials.

Author Information Reprints and permissions information is available at www.nature.com/reprints. The authors declare no competing financial interests. Readers are welcome to comment on the online version of the paper. Correspondence and requests for materials should be addressed to Y.D. (ypdu@nankai.edu.cn), B.H. (bolong.huang@polyu.edu.hk) or D.S. (dongsu@iphy.ac.cn).

Methods

Materials. Graphite (nanoparticle, natural, thickness: 40 nm, lateral size: 400-600 nm) was purchased from ACS Material Store and used without any further purification. The solvents of

ethanol, dimethyl carbonate (DMC) and N-methyl-2-pyrrolidone (NMP) were in ACS reagent grade and were purchased from Fisher Scientific and used without further purification.

TEM Characterization. The in-situ TEM electrochemical dry cell was incorporated into a Nanofactory TEM-STM specimen holder (shown in Figure 2a), in which graphite dispersed onto a TEM half-grid with amorphous carbon support are analogous to the active electrode. The lithium metal is coated onto a piezo-driven tungsten (W) probe, which acts as the counter electrode. The graphite and Li were loaded onto the holder in an Ar-filled glove box, and the sample holder is transferred from an Ar-filled sealed container to the microscope within several seconds. During those seconds, a thin layer of Li_2O is formed on Li metal, which could be used as the solid electrolyte in the dry cell. During the in-situ lithiation, a constant negative DC potential (1.5 V) was applied to the specimen, and the lithiation processes were captured by real-time imaging in SAED mode with a JEM-2100F transmission electron microscope (JEOL) at an acceleration voltage of 200 kV. Electron-energy loss spectroscopy (EELS) was conducted on JEM-2100F operated at 200 kV. In order to make the electron beam below the threshold of damage the C atoms in graphite, the in-situ HRTEM image was obtained in a Titan 80-300 transmission electron microscope (FEI) at an acceleration voltage of 80 kV[37], which has an objective-lens aberration corrector and a spatial resolution of 1.5 Å in the high-resolution phase-contrast mode. The ex-situ samples after discharge in coin cells were examined accordingly.

Electrochemical Measurement. The electrodes were prepared with 90 wt % active material (graphite), 5 wt % acetylene carbon black, and 5 wt % polyvinylidene fluoride (PVDF) in N-methyl-2-pyrrolidone (NMP) and cast onto copper foil current collectors using a doctor blade. The electrodes were dried in the dry room at room temperature for 24 hours. The 2032-type coin cells were assembled in an argon-filled glove box using the composite electrode as the

positive electrode and Li metal as the negative, electrode with Celgard (2325) separator in between to prevent shorting. The electrolyte was lithium hexafluorophosphate ($LiPF_6$) (1M) in ethylene carbonate/dimethyl carbonate (EC/DMC) (volume ratio 50:50). The electrochemical measurements were conducted at room temperature using a Biologic (VMP3) battery cycler. The cells were cycled galvanostatically at 0.1 C and 10 C between 0.01 and 3.0 V, respectively.

XRD/Raman Characterization. The X-ray diffraction (XRD) patterns were collected on Ultima III XRD/XRR diffractometer (Cu Kα radiation, λ = 1.54056 Å) at room temperature. The samples after discharge (0.1 C-rate/10 C-rate after 10 cycles) were sealed in 0.5 mm thickness scotch tape inside the glovebox, and diffraction patterns were measured in a 2θ range = 15-45° with a step size of 0.01° and step speed of 1°/min. The zinc powders (6-8 micron, $P6_3/mmc$ space group) were used as the reference peaks to demonstrate that the graphite peak shifting was electrochemical in nature not an artifact of mechanical tests. Additional analysis was performed by Raman spectroscopy (WiT37ec Probe Microscope) using 532 nm laser radiation.

Calculation setup. In this molecule dynamic simulation, CASTEP codes[38] with Broyden-Fletcher-Goldfarb-Shannon (BFGS) algorithm was selected for geometry optimization during the dynamic simulations [1]. The cut-off energy for PBE[39] with GGA[40,41] functions is set to be 750 eV with a plane-wave basis set. The model of graphite inserted with lithium atom is a 7×7×2 supercell of graphite with 392 carbon atoms. To discover the dynamic simulation with different situations, we have applied disorder lithium atom models in the graphite model with 78 lithium atoms randomly distributed among four layers of graphite. For dynamic simulation, we choose NVT (*i.e. a dynamic study at fixed volume with a thermostat to maintain a constant temperature*) mode under 300K with constant volume. Each step has been set as 1 fs in the

disorder models. For the NPT (*i.e. a dynamic study with a thermostat to maintain a constant temperature and with a barostat to maintain a constant pressure*) mode, the dynamic simulation environment has been set at 300K with constant pressure. NPT model has applied the electric field of 1.5 V/m on [010] direction to observe the influence of the external electric field. NVT model has been operated under non-electrical field condition and same electrical field condition as NPT.

For all the defect formation, a 4×4×1 graphite unit cell has been constructed to build the defect in the cell for geometry optimization. For geometry optimization of the defective structure and distorted graphite unit cell, a 380 eV with ultrasoft pseudopotential setting has been chosen. Within this setting, the maximum energy on every atom is 5×10^{-5} eV with max force 0.1 eV/Å.

Online Content Additional Supplementary Data display items and Source Data, are available in the online version of the paper; references unique to these sections appear only in the online paper.

References

1. Kaskhedikar, N. A. & Maier, J. Lithium storage in carbon nanostructures. *Adv. Mater.* **21**, 2664-2680 (2009).
2. Dahn, J. R., Zheng, T., Liu, Y. & Xue, J. S. Mechanisms for lithium insertion in carbonaceous materials. *Science* **270**, 590-593 (1995).
3. Dahn, J. R. Phase diagram of Li_xC_6. *Phys. Rev. B* **44**, 9170-9177 (1991).
4. Okamoto, Y. Density functional theory calculations of alkali metal (Li, Na, and K) graphite intercalation compounds. *J. Phys. Chem. C* **118**, 16-19 (2013).
5. Konar, S., Häusserman, U. & Svensson, G. Intercalation compounds from LiH and graphite:

relative stability of metastable stages and thermodynamic stability of dilute stage I_d. *Chem. Mater.* **27**, 2566-2575 (2015).

6. Dimiev, A. M. et al. Direct real-time monitoring of stage transitions in graphite intercalation compounds. *ACS Nano* **7**, 2773-2780 (2013).
7. Sacci, R. L., Gill, L. W., Hagaman, E. W., & Dudney, N. J. Operando NMR and XRD study of chemically synthesized LiC_x oxidation in a dry room environment. *J. Power Sources* **287**, 253-260 (2015).
8. Bao, W. et al. Approaching the limits of transparency and conductivity in graphitic materials through lithium intercalation. *Nat. Commun.* **5**, 1-9 (2014).
9. Wang, X. L. et al. Visualizing the chemistry and structure dynamics in lithium-ion batteries by in-situ neutron diffraction. *Sci. Rep.* **2**, 747 (2012).
10. Hofmann, U. & Rüdorff, W. The formation of salts from graphite by strong acids. *Trans. Faraday Soc.* **34**, 1017-1021 (1938).
11. Dresselhaus, M. S. & Dresselhaus, G. Intercalation compounds of graphite. *Adv. Phys.* **30**, 139-326 (1981).
12. Daumas, N. & Herold, A. Sur les relations entre la notion de stade et les mecanismes reactionnels dans les composes d'insertion du graphite. *Comptes Rendus Acad. Sci. Ser. C* **268**, 373-375 (1969).
13. Timp, G. & Dresselhaus, M. S. The ultramicrostructure of commensurate graphite intercalation compounds. *J. Phys. C: Solid State Phys.* **15**, 2641-2651 (1984).
14. Buqa, H. et al. High rate capability of graphite negative electrodes for lithium-ion batteries. *J. Electrochem. Soc.* **152**, 474-481, (2005).
15. Gavilán-Arriazu, E. M. et al.The kinetic origin of the Daumas-Hérold model for the Li-

ion/graphite intercalation system. *Electrochem. Commun.* **93**, 133-137 (2018).

16. Liu, Q. et al. Understanding undesirable anode lithium plating issues in lithium-ion batteries. *RSC Adv.* **6**, 88683-88700 (2016).

17. Uhlmann, C. et al. In situ detection of lithium metal plating on graphite in experimental cells. *J. Power Sources* **279**, 428-438 (2015).

18. Sethuraman, V. A., Hardwick, L. J., Srinivasan, V. & Kostecki, R. Surface structural disordering in graphite upon lithium intercalation/deintercalation. *J. Power Sources* **195**, 3655-3660 (2010).

19. Kühne, M. et al. Reversible superdense ordering of lithium between two graphene sheets. *Nature* **564**, 234-239 (2018).

20. Arora, P., Doyle, M. & White, R. E. Mathematical modeling of the lithium deposition overcharge reaction in lithium-ion batteries using carbon-based negative electrodes. *J. Electrochem. Soc.* **10**, 3543-3553 (1999).

21. Huang, J. Y. et al. In situ observation of the electrochemical lithiation of a single SnO_2 nanowire electrode *Science* **330**, 1515-1520 (2010).

22. He, K. et al. Visualizing non-equilibrium lithiation of spinel oxide via in situ transmission electron microscopy. *Nat. Commun.* 7, 11441 (2016).

23. Wen, Y. et al. Expanded graphite as superior anode for sodium-ion batteries *Nat. Commun.* **5**, 4033 (2014).

24. Sharma, N. & Peterson, V. K. Overcharging a lithium-ion battery: Effect on the Li_xC_6 negative electrode determined by in situ neutron diffraction. *J. Power Sources* **244**, 695-701 (2013).

25. Mironov, B. E. et al. Electron irradiation of nuclear graphite studied by transmission

electron microscopy and electron energy loss spectroscopy. *Carbon* **83**, 106-117 (2015).

26. Meyer, J. C. et al. Accurate measurement of electron beam induced displacement cross sections for single-layer graphene. *Phys. Rev. Lett.* **108**, 196102 (2012).
27. Yoo, E. et al. Large reversible Li storage of graphene nanosheet families for use in rechargeable lithium ion batteries. *Nano Lett.* **8**, 2277-2282 (2008).
28. Buiel, E. & Dahn, J. R. Li-insertion in hard carbon anode materials for Li-ion batteries. *Electrochimica Acta* **45**, 121-130 (1999).
29. Scherrer, P. Estimation of size and internal structure of colloidal particles by means of Röntgen rays. *Göttinger Nachrichten Math. Phys.* **2,** 96-100, (1918).
30. Li, Z. Q. et al. X-ray diffraction patterns of graphite and turbostratic carbon. *Carbon* **45**, 1686-1695 (2007).
31. Tuinstra, F. & Koenig, J. L. Raman spectrum of graphite. *J. Chem. Phys.* **53**, 1126-1130 (1970).
32. Cançado, L. G. et al. General equation for the determination of the crystallite size L_a of nanographite by Raman spectroscopy. *Applied Phys. Lett.* **88**, 163106 (2006).
33. Kobayashi, Y., Fukui, K. I., Enoki, T., Kusakabe, K. & Kaburagi, Y. Observation of zigzag and armchair edges of graphite using scanning tunneling microscopy and spectroscopy. *Phys. Rev. B* **71**, 193406 (2005).
34. Holzwarth, N. A. W., Louie, S. G. & Rabii, S. Lithium-intercalated graphite: self-consistent electronic structure for stages one, two, and three. *Phys. Rev. B* **28**, 1013-1025 (1983).
35. Meunier, V., Kephart, J., Roland, C. & Bernholc, J. *Ab initio* investigations of lithium diffusion in carbon nanotube systems. *Phys. Rev. Lett.* **88**, 075506 (2002).
36. Yan, J. et al. A novel perspective on the formation of the solid electrolyte interphase on the

graphite electrode for lithium-ion batteries. *Electrochimica Acta* **55**, 1785-1794 (2010).

37. Meyer, J. C. et al. Accurate measurement of electron beam induced displacement cross sections for single-layer graphene. *Phys. Rev. Lett.* **108**, 196102, (2012).

38. Clark, S. J. et al. First principles methods using CASTEP. *Zeitschrift Fur Kristallographie* **220**, 567-570, (2005).

39. Head, J. D. & Zerner, M. C. A broyden-fletcher-goldfarb-shanno optimization procedure for molecular geometries. *Chem. Phys. Lett.* **122**, 264-270 (1985).

40. Perdew, J. P., Burke, K. & Ernzerhof, M. Generalized gradient approximation made simple. *Phys. Rev. Lett.* **77**, 3865-3868 (1996).

41. Perdew, J. P. et al. Atoms, molecules, solids, and surfaces: Applications of the generalized gradient approximation for exchange and correlation. *Phys. Rev. B* **46**, 6671-6687 (1992).

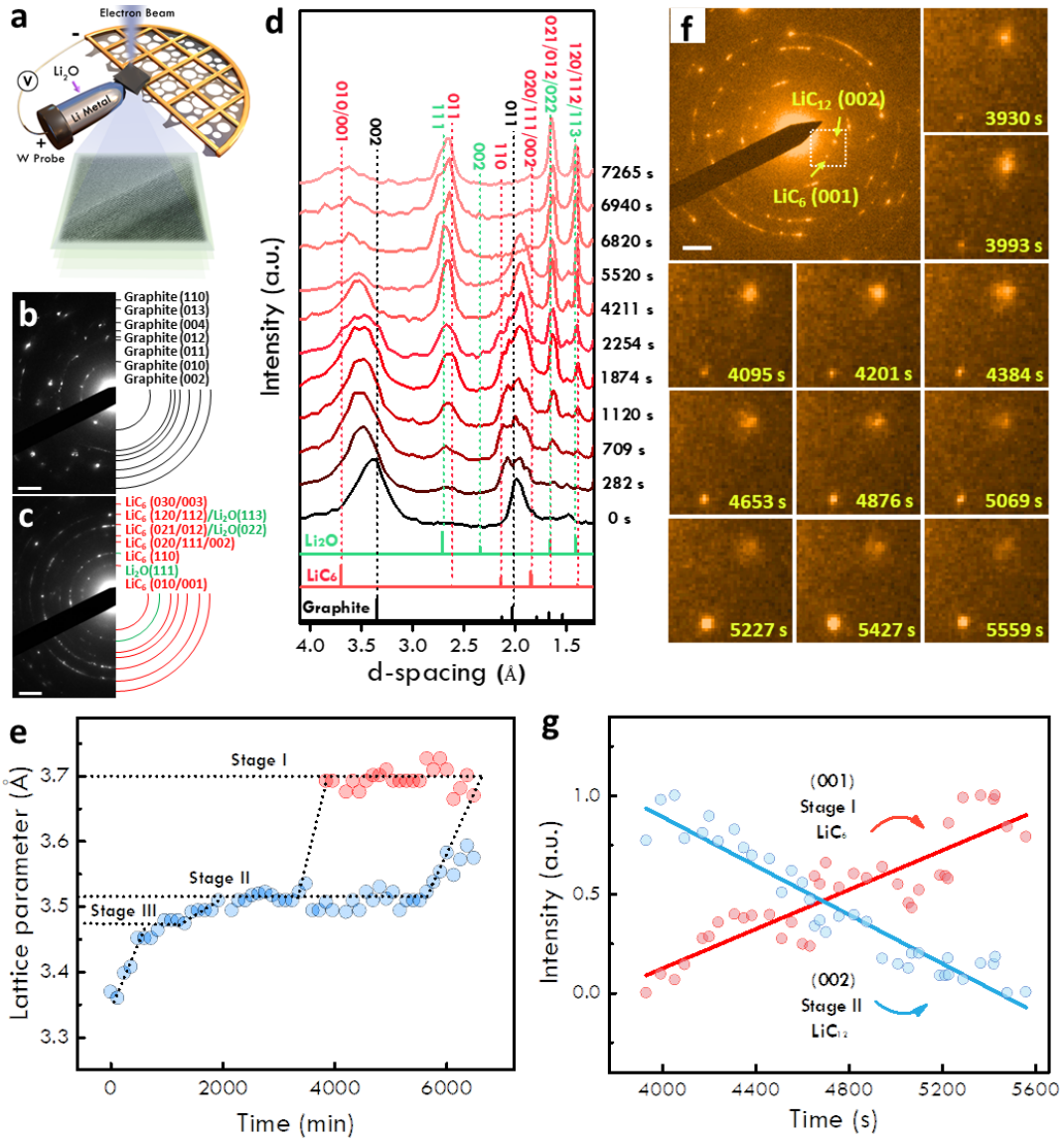

Fig. 1 | Phase evolution by in-situ electron diffraction. (a) Schematic illustration of the in-situ TEM experimental setup. The SAED patterns of (b) fully lithiated (7265 s) state and (c) pristine graphite (0 s). (d) Integrated intensity profiles of the diffraction patterns in time-sequence from 0 to 7265 s, where black, red and green lines indicate the peaks of graphite, LiC_6, and Li_2O phases, respectively. (e) The SAED patterns of lithiated states showing the LiC_6 (001) and LiC_{12} (002) phases evolution during lithiation. Scale bars of b, c and e are 2 1/nm. (f) Lattice parameter's change measured from pristine graphite (002) to reflections of LiC_x in a function of time. (g) Intensity change of two selected reflections of LiC_6 (001) and LiC_{12} (002) from Fig. 1e. Bragg reflections during lithiation, indicating the stage phases evolution of graphite intercalation.

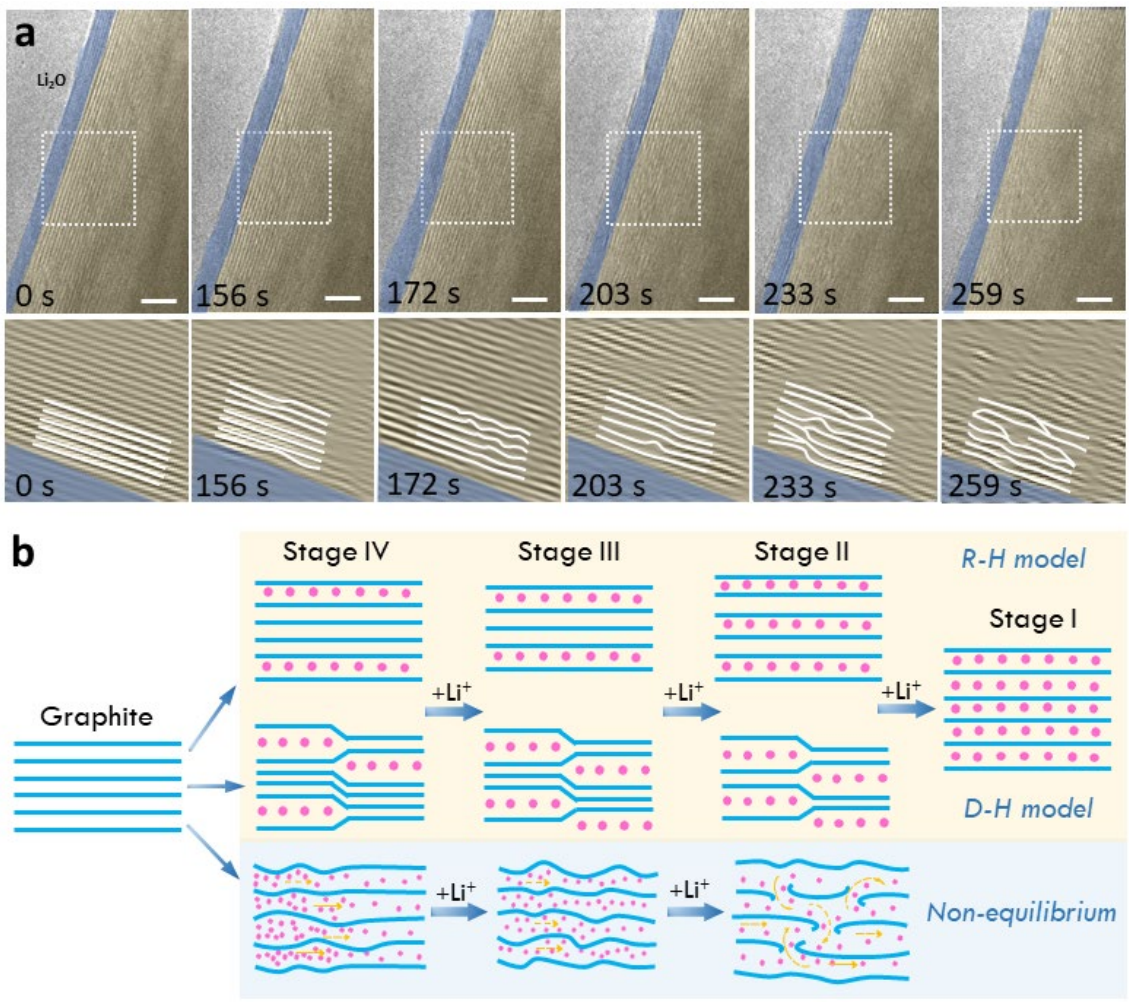

Fig. 2 | Structural evolution during in-situ lithiation of graphite. (a) In-situ HRTEM images and corresponding filtered TEM images showing the d-spacing expansion and interlayer distortion during lithiation. Bottom: inverse fast Fourier transform (IFFT) images. Scale bars of a are 5 nm. (b) Schematic of equilibrium (R-H model and D-H model) and non-equilibrium lithiation process during the Li-ions insertion into the graphite layers. The blue lines are the graphite layers and the red balls are layers of lithium insertion.

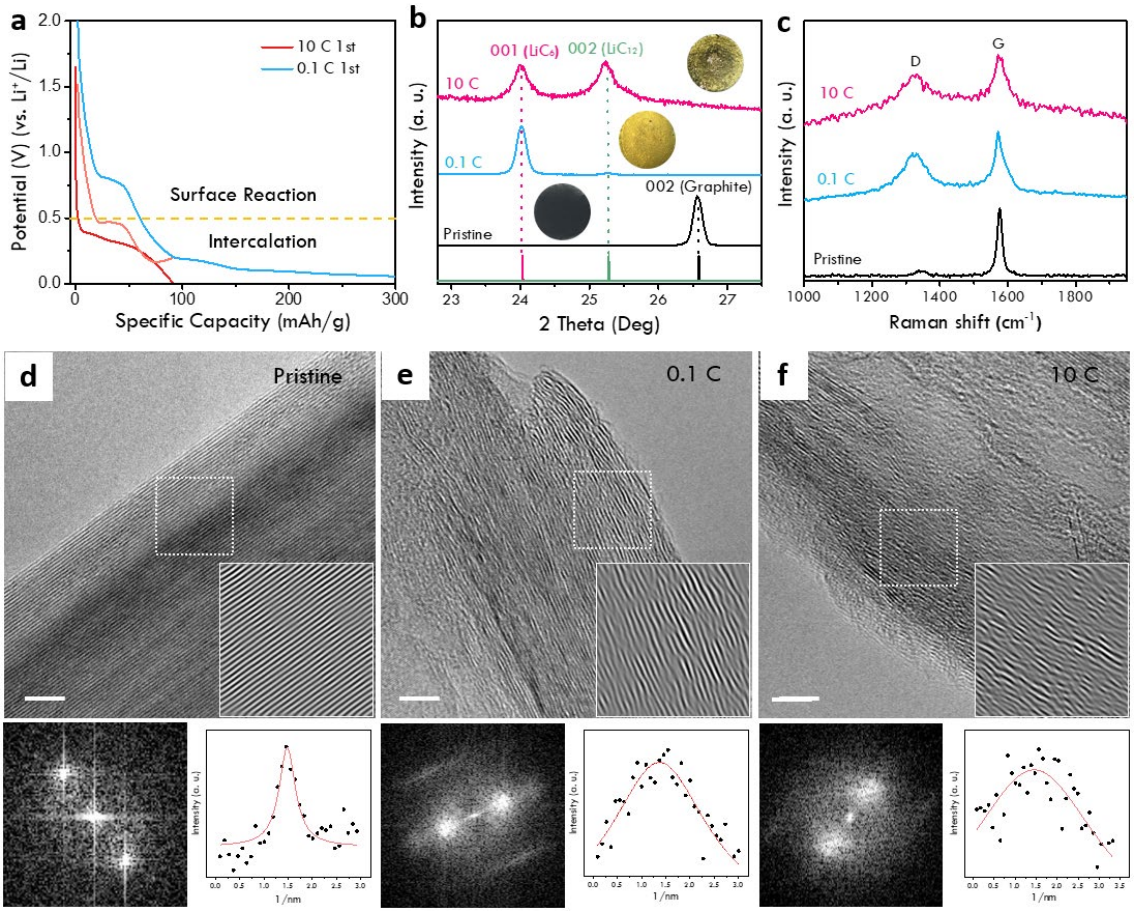

Fig. 3 | Structural change of graphite in the coin cell. (a) First cyclic discharge curves of the graphite electrode in the range of 0.01-3.00 V at rates of 0.1 C and 10 C. (b) Ex-situ XRD and (c) Raman spectra of pristine, 0.1 C-rate and 10 C-rate lithiation after 10 cycles. Inset showing the photographs of pristine graphite, 0.1 C-lithiated and 10 C-lithiated electrodes, respectively. HRTEM images for (d) pristine, (e) 0.1 C-rate and (f) 10 C-rate lithiation after 10 cycles. Inset showing the IFFT images of pristine, 0.1 C-rate and 10 C-rate lithiation after 10 cycles. Bottom: FFT results and the intensity profiles of Bragg reflection from FFT with Lorentz fitting, enlarging the full width at half maximum (FWHM) with increasing of the current rate. Scale bars of d, e and f are 5nm.

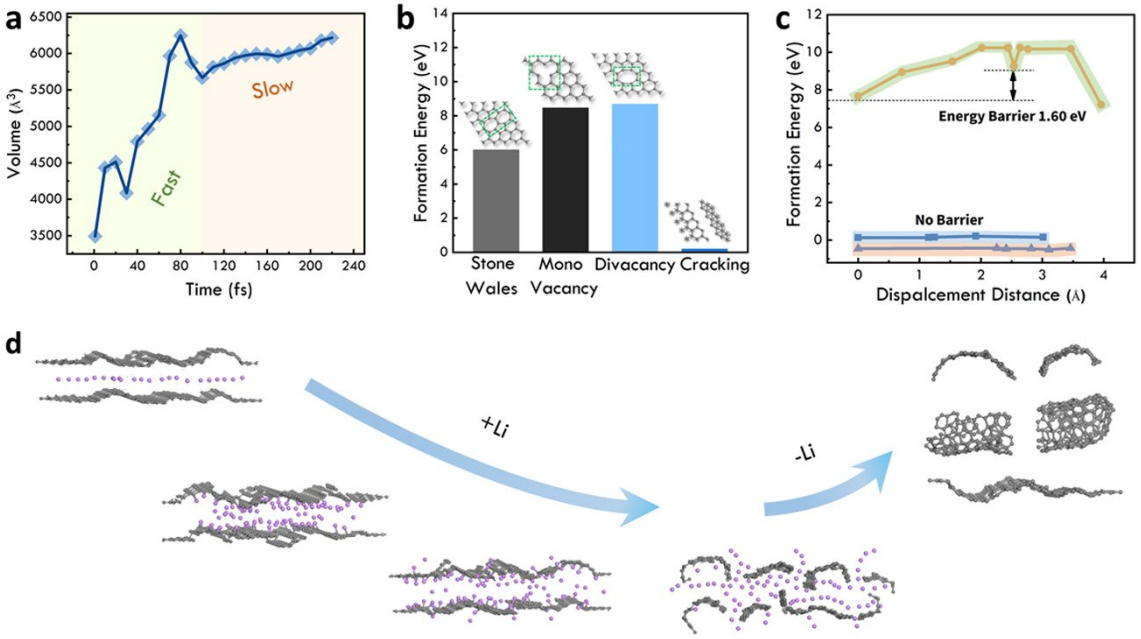

Fig. 4 | DFT-MD calculations on the lithiation/delithiation of graphite. (a) Volume expansion trend of graphite with randomly distributed Li atoms under 1.5 V electrical field on (010) direction. (b) Comparison of different defect formation in graphite. Inset showing the schematic of different Li-ion transmission model during intercalation of Li atoms into graphite. (c) The energy barrier of interlayer Li atoms migration through defects between divacancy and cracking. (d) Schematic diagrams of the non-equilibrium lithiation/delithiation process, the inset is HRTEM image after 10 cycles showing “Fullerenalization” structure, scare bar is 5 nm.